Microwave photo-association of fine-structure-induced Rydberg $(n+2)D_{5/2}nF_J$ macro-dimer molecules of cesium

Jingxu Bai,[1] Yuechun Jiao ⬚,[1,2,*] Rong Song,[1] Georg Raithel ⬚,[3,†] Suotang Jia,[1,2] and Jianming Zhao ⬚[1,2,‡]

[1]*State Key Laboratory of Quantum Optics and Quantum Optics Devices, Institute of Laser Spectroscopy,*
Shanxi University, Taiyuan 030006, China

[2]*Collaborative Innovation Center of Extreme Optics, Shanxi University, Taiyuan 030006, China*

[3]*Department of Physics, University of Michigan, Ann Arbor, Michigan 48109-1120, USA*

Long-range $(n+2)D_{5/2}nF_J$ Rydberg macro-dimers are observed in an ultracold cesium Rydberg gas for $39 \leqslant n \leqslant 48$. Strong dipolar flip ($\langle D_{5/2}F_{5/2}|\hat{V}_{dd}|F_{5/2}D_{5/2}\rangle$, $\langle D_{5/2}F_{7/2}|\hat{V}_{dd}|F_{7/2}D_{5/2}\rangle$) and cross ($\langle D_{5/2}F_{7/2}|\hat{V}_{dd}|F_{5/2}D_{5/2}\rangle$) couplings lead to bound, fine-structure-mixed $(n+2)D_{5/2}nF_J$ macro-dimers at energies between the F_J fine-structure levels. The $(n+2)D_{5/2}nF_J$ macro-dimers are measured by microwave photo-association from optically prepared $[(n+2)D_{5/2}]_2$ Rydberg-pair precursor states. Calculated adiabatic potential curves are used to elucidate the underlying physics and to model the macro-dimer spectra, with good overall agreement. Microwave photo-association allows Franck-Condon tuning, which we have studied by varying the detuning of a Rydberg-atom excitation laser. Further, in Stark spectroscopy, we have measured molecular DC electric polarizabilities that are considerably larger than those of the atomic states. The large molecular polarizabilities are unexpected and may be caused by high-ℓ mixing. The observed linewidths of the Stark-shifted molecular lines provide initial evidence for intramolecular induced-dipole-dipole interaction.

I. INTRODUCTION

Ultracold gases in the μK regime have opened an avenue into the investigation of interacting many-body systems. While interactions between ultracold ground-state atoms generally remain fairly weak, interactions involving Rydberg atoms (atoms with principal quantum numbers $n \gtrsim 10$) are readily observable in typical cold atomic gases. Molecules in which a ground-state atom is located inside the Rydberg atom [1–10] have attracted considerable attention due to their permanent electric dipole moments [7,8]. Rydberg-atom-ion molecules, which were predicted and observed [11–14], are bound by electric multipolar interactions, as are molecules consisting of two Rydberg atoms. The latter, known as Rydberg macro-dimers, were predicted in Ref. [15] and observed, for instance, in Refs. [16–22]. Rydberg-pair interactions, which include the dipole-dipole ($\sim n^4/R^3$) [23,24] and the van der Waals ($\sim n^{11}/R^6$) [25–27] interactions (R is the internuclear distance), give rise to long-range adiabatic potential curves. Some of these have wells that support meta-stable Rydberg-pair macro-dimer molecules.

Photo-association is widely used in the preparation of Rydberg macro-dimers. Deiglmayr *et al.* [17] have prepared Cs macro-dimer molecules near $nS\,n'F$ and $[nP]_2$ asymptotes for $22 \leqslant n \leqslant 32$, and near $nP\,(n+1)S$ for $n = 43$ and 44 [18], where molecules are bound through long-range dipolar interaction. Han *et al.* [19] have reported on $[62D]_2$ macro-dimer molecules prepared via a two-color, two-photon photo-association scheme and have modeled their results using molecular-potential computations [24]. Hollerith *et al.* [20–22,28] observed Rydberg macro-dimers with bond lengths up to 0.7 μm in optical lattices using a quantum gas microscope, manipulated the molecular arrangement, proposed applications in quantum computing, and recently observed macro-trimerons.

Here, we observe fine-structure-mixed (FS-mixed) long-range $(n+2)D_{5/2}nF_J$ Rydberg macro-dimer molecules. These are bound by dipolar interactions, which drop off as n^4/R^3 as a function of the internuclear distance R and are the longest-range multipole coupling between neutrals. We use a microwave instead of the more commonly employed laser photo-association approach, allowing us to access F-type Rydberg molecules with only two lasers. The microwave field excites optically prepared $[(n+2)D_{5/2}]_2$ precursor Rydberg pairs, which are relatively weakly interacting via repulsive n^{11}/R^6 van der Waals potentials, into more strongly interacting $(n+2)D_{5/2}nF_J$ macro-dimer states. At large separation $R \gtrsim 10\,\mu m$, the $(n+2)D_{5/2}nF_J$ potentials are FS split by several tens of megahertz. With decreasing R, the FS-split $(n+2)D_{5/2}nF_J$ potentials rapidly spread to both lower and higher energies due to dipolar C_3/R^3 interactions, and they eventually interpenetrate within the energy range between the
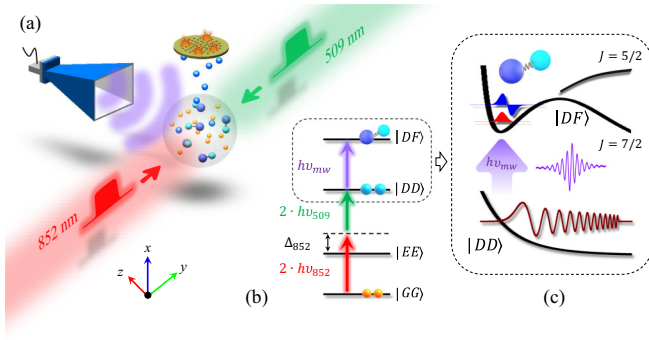
FIG. 1. (a) Sketch of the experimental setup. Rydberg macro-dimer molecules are produced by laser excitation of D-state Rydberg atoms and microwave photo-association. (b) Level diagram. A Rydberg pair, $|DD\rangle = [(n+2)D_{5/2}]_2$, is laser-excited from $|GG\rangle = [6S_{1/2}]_2$ by 852 and 509 nm lasers (852 nm laser detuning $\Delta_{852}/2\pi = 360$ MHz). A scanned microwave field excites nF_J atoms or photo-associates $|DF\rangle = (n+2)D_{5/2}\,nF_J$ fine-structure (FS)-mixed macro-dimers, which are detected as described in the text. (c) Visualization of microwave photo-association with incident and bound vibrational wave functions on respective potential curves.

atomic nF_J FS levels. The intersecting potential energy curves are coupled via dipolar cross couplings between molecular states involving both J values of the nF_J doublet. The cross couplings are fairly strong and also scale as $1/R^3$. These properties, in combination with the relatively small FS splitting of the nF_J levels, lead to comparatively large macro-dimers in several potential wells that are robust against nonadiabatic decay. In this paper, we further consider Franck-Condon tuning afforded by microwave photo-association spectroscopy and suggest methods of how to use Franck-Condon tuning more effectively in future work. Finally, we investigate the Stark effect of $(n+2)D_{5/2}\,nF_J$ macro-dimer signals. The molecular Stark shifts are found to be substantial, as they reflect the large polarizability of the F-type Rydberg constituents. Somewhat surprisingly, the measured molecular Stark shifts exceed a perturbative prediction by a factor of 2.5, an observation that awaits a future explanation. The widths of molecular Stark lines hint at intramolecular induced-dipole-dipole interaction within individual Rydberg molecules. This effect, which to our knowledge has not been reported in Rydberg macro-dimers, likely is elicited by large induced intramolecular dipoles of the constituent atoms.

II. EXPERIMENTAL SCHEME

The experiment is performed using a Cs magneto-optical trap with a peak density of $\sim 10^{10}\ \mathrm{cm^{-3}}$ and a temperature of $\sim 40\,\mu$K after molasses cooling. After switching off the trap laser, $[(n+2)D_{5/2}]_2$ Rydberg-pair precursor states are prepared by 4 photon excitation via coincident and counter-propagating 852 and 509 nm laser pulses of $1\,\mu$s duration, as shown in Fig. 1(a). Rydberg-atom pairs are then photo-associated into $(n+2)D_{5/2}nF_J$ macro-dimers by a $20\,\mu$s microwave pulse. An electric field ramp is then applied for state-selective field ionization [25]. Time-resolved detection of the liberated ions with a microchannel plate detector and a boxcar integrator then allows selective detection of nF-type

Rydberg atoms and molecular constituents. Prior to the experiment, we employ Stark and Zeeman spectroscopy to reduce stray electric and magnetic fields to <2 mV/cm and 5 mG, respectively. More experimental details are given in Ref. [29].

III. POTENTIAL ENERGY CURVES

To model the experimental spectra, we consider the product Hilbert space of two Rydberg atoms and add the multipole interaction between the atoms to the unperturbed two-body Hamiltonian. The molecular potential energy curves are obtained by diagonalization of the Rydberg-pair Hamiltonian within basis subsets of states with conserved M, defined as the sum of the projections of the total electronic angular momenta onto the internuclear axis, and conserved parity p, which depends on whether the sum of the orbital electronic angular momenta is even or odd [30]. We include multipolar interactions up to order $L_a + L_b = 6$, with the dipole, quadrupole, etc., terms for atoms a and b denoted $L_a = 1, 2, \ldots$ and $L_b = 1, 2, \ldots$.

The multipole interactions scale as $\bar{n}^{2(L_a+L_b)}R^{1+L_a+L_b}$, where R is the internuclear distance and $\bar{n}$ the average principal quantum number of the Rydberg-pair states of interest. The leading interaction of a pair of atoms in states $a = (n+2)D_{5/2}$ and $b = nF_J$, which are of main interest in this paper, is the dipole-dipole interaction, which scales as n^4/R^3. The interactions drop rapidly with increasing order $L_a + L_b$. The multipole range $2 \leqslant L_a + L_b \leqslant 6$ used in our calculations is generous. More details describing our calculations are found in Refs. [19,24].

For each M and p, the computation yields sets of adiabatic potential energy curves vs R, with corresponding symmetrized adiabatic Rydberg-pair wave-functions. The latter are of the form:

$$|\psi_{\mathrm{mol}}(R)\rangle = \frac{1}{\sqrt{2}} \sum_{\lambda_a \lambda_b} c_{\lambda_a, \lambda_b}(R)$$
$$\times [|\lambda_a \lambda_b\rangle - p(-1)^{\ell_a + \ell_b}|\lambda_b \lambda_a\rangle], \quad (1)$$

with $\lambda_{a(b)} = |n_{a(b)}, \ell_{a(b)}, J_{a(b)}, m_{J_{a(b)}}\rangle$ denoting single-atom states in the molecular frame of reference. The sum is restricted to $m_{J_a} + m_{J_b} = M$. The coefficients c_{λ_a, λ_b}, which depend on the internuclear separation R and on a suppressed index for the molecular potentials, reflect details on molecular configuration and FS mixing.

In Fig. 2(a), we show calculated adiabatic potentials for Cs Rydberg pair states in $39D_{5/2}\,37F_J$ for the indicated values of M and p. The detuning is defined to be zero at the $39D_{5/2}\,37F_{5/2}$ asymptote. We include one-body Rydberg states with $\ell \leqslant 7$, $|m_J| \leqslant 7.5$, and effective quantum number $32.9 \leqslant n_{\mathrm{eff}} \leqslant 40.1$. Further, the two-body product space is limited to all pairs with unperturbed energy defects $|\Delta_2| \leqslant h \times 30$ GHz relative to the $39D_{5/2}\,37F_{5/2}$ asymptote. In Fig. 2(b), we show the measured photo-association spectrum vs microwave detuning. The narrow and wide features in (b) near zero and near -20 MHz detuning show the $39D_{5/2} \to 37F_{5/2}$ and $39D_{5/2} \to 37F_{7/2}$ atomic resonances, which are broadened due to dipolar Rydberg-pair interactions. About halfway between the atomic resonances, the spectrum in Fig. 2(b) exhibits a narrow signal that coincides with
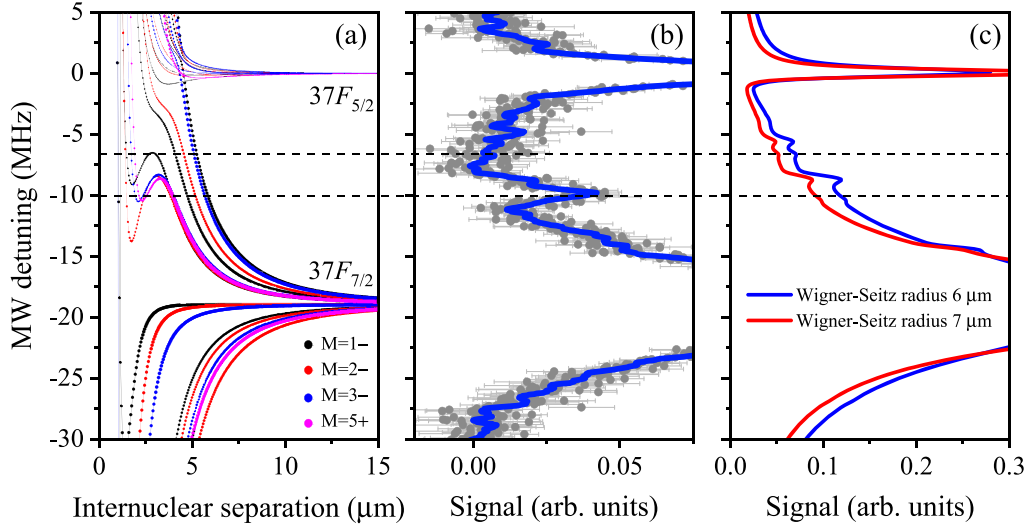
FIG. 2. (a) Calculated potential energy curves vs internuclear separation R for $39D_{5/2}\,37F_J$ pairs with the indicated conserved values for $M = m_{J_a} + m_{J_b}$ and for the parity ($-/+$ means odd/even). Symbol areas are proportional to calculated microwave transition rates from the precursor state $[39D_{5/2}]_2$. (b) Experimental microwave spectrum, averaged over 50 measurements. Error bars denote standard error of the mean (SEM). In (a), between $37F_{7/2}$ and $37F_{5/2}$, we find molecular potential wells that correspond with signals measured in (b). These signatures reflect fine-structure (FS)-mixed $39D_{5/2}\,37F_J$ macro-dimers. Dashed horizontal lines across (a) and (b) mark the detunings of prominent potential maxima and minima. (c) Simulated microwave spectra for two Wigner-Seitz radii, showing good qualitative agreement with (b).

Rydberg-dimer potential wells seen in Fig. 2(a), as indicated with the dashed lines.

At large distances ($R \gtrsim 8\,\mu\text{m}$ in Fig. 2), the dipole-dipole interactions are dominant and lead to asymptotic potentials $\propto C_3/R^3$. The C_3 coefficients are much larger for $(n+2)D_{5/2}\,nF_{7/2}$ than for $(n+2)D_{5/2}\,nF_{5/2}$ due to differences in angular matrix elements. Averaged over all M and parities, the magnitudes of the C_3 coefficients average to ~ 1.3 and $\sim 0.07\,\text{GHz}\,\mu\text{m}^3$ for the $37F_{7/2}$ and $37F_{5/2}$ resonances, respectively. Also, the respective 96 and 72 long-range potentials are fairly evenly distributed and symmetric about the asymptotic energies. As a result, the interaction-broadened atomic $37F_J$ lines in Fig. 2(b) are quite symmetric, with the $F_{7/2}$ line being wider than the $nF_{5/2}$ line by a factor of ~ 5.

The potential wells in Fig. 2(a) at $R \sim 2\,\mu\text{m}$ correlate with signal maxima in the experimental data in Fig. 2(b). To explain their origin, we first note that the strongest interactions are the resonant flip interactions between (symmetrized) $|39D_{5/2}, 37F_{7/2}\rangle$ pair states, which have dipole-dipole matrix elements $V_{7/2} := \langle DF_{7/2}|\hat{V}_{dd}|F_{7/2}D\rangle$ and cause the aforementioned massive broadening of the atomic $F_{7/2}$ line. The matrix elements of the $|39D_{5/2}, 37F_{5/2}\rangle$ flip interactions, $V_{5/2} := \langle DF_{5/2}|\hat{V}_{dd}|F_{5/2}D\rangle$, are only ~ 0.05 times as strong, resulting in a less-broadened atomic $F_{5/2}$ line. With decreasing R, numerous $39D_{5/2}\,37F_{7/2}$ potentials push upward into comparatively weakly shifting $39D_{5/2}\,37F_{5/2}$ potentials and intersect, generating a series of anticrossings. The couplings at these anticrossings involve products of two electric-dipole matrix elements between $39D_{5/2}$ and $37F_J$ FS components, with one matrix element for $J = \frac{5}{2}$ and the other for $J = \frac{7}{2}$. As a result, the cross couplings have strengths on the order of $\sqrt{V_{7/2}V_{5/2}}$, which amounts to about a quarter of the atomic FS splitting for the macro-dimer molecules of interest in this paper. With all relevant couplings being dipolar and hence relatively strong,

the potential wells that result for several M's and parities are well distinct and robust. The vibrational states in the wells are likely stable against nonadiabatic decay, as suggested by our experimental observations of sharp $(n+2)D_{5/2}\,nF_J$ macro-dimer features.

To prove the FS-mixed character of the observed macro-dimers, we have computed the expectation value $s(R) = \langle J - \ell\rangle(R)$ of adiabatic electronic states [see Eq. (1)] for several potential curves in Fig. 2(a) that have wells. Since $s = \pm\frac{1}{2}$ for $J = \ell + \frac{1}{2}$ and $J = \ell - \frac{1}{2}$, $s(R)$ is a measure for the R dependence of the FS mixing. As an example, in Fig. 3, we show $s(R)$ for the $M = 3$, $p = -1$ macro-dimer potential that has a potential well supporting bound states. At large R outside the well, it is $s(R) \approx \frac{1}{2}$, which shows that, outside the well, the pair state $|\psi_{\text{mol}}\rangle$ from Eq. (1) has the character $[39D_{5/2}\,37F_{7/2}]$. Inside the well, $s(R)$ drops to ~ 0.1, indicating that $|\psi_{\text{mol}}\rangle$ is an approximately even superposition of $[39D_{5/2}\,37F_{7/2}]$ and $[39D_{5/2}\,37F_{5/2}]$ contributions. As seen in Fig. 3, the FS mixing is most pronounced at the potential minimum at $R \sim 2\,\mu\text{m}$, and it diminishes again near the inner turning point of the potential well. The same physics applies to the other potential wells in Fig. 2(a).

For further discussion, we note that the FS-mixed $(n+2)D_{5/2}\,nF_J$ molecular-potential wells are squeezed inside the narrow spectral range between the atomic nF_J states, which are only a few tens of megahertz apart (for $n \sim 40$). The proximity of the atomic FS states is instrumental in pushing the radial positions of the FS-mixed potential wells far out along R, leading to particularly long-range macro-dimer states. Also, intersections with other, potentially unaccounted-for potentials become increasingly unlikely with increasing R, and if there were any, the intersecting potentials would likely be too weakly coupled to cause fast nonadiabatic decay.
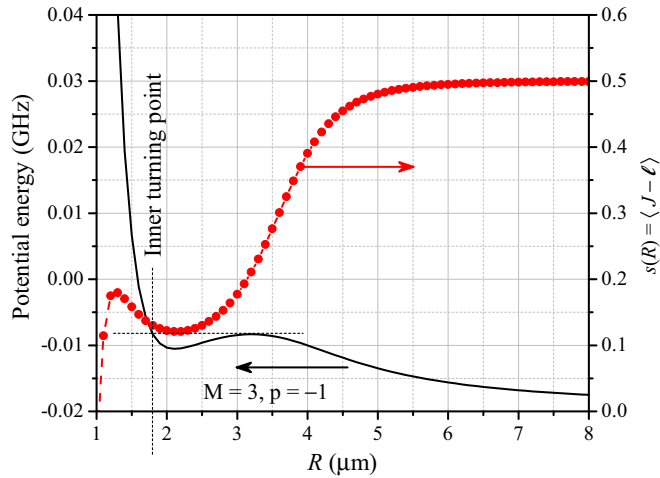
FIG. 3. Fine-structure mixing in $39D_{5/2}37F_J$ macro-dimer. Solid black line: Adiabatic potential curve for $M = 3$, $p = -1$ that supports bound macro-dimer states. Red symbols: Expectation value of $s(R) = \langle J - \ell \rangle(R)$ vs R. The adiabatic electronic state varies from coaligned coupling between spin and orbital angular momenta at large R to mixed coupling within the molecular potential well.

IV. MICROWAVE EXCITATION RATES OF MACRO-DIMERS

We model our measured photo-association spectra, such as the one shown in Fig. 2(b), following the methods described in Refs. [19,24]. We rotate the states $|\psi_{\text{mol}}\rangle$ of Eq. (1) from the molecular into the frame of reference of the microwave field using (reduced) rotation operators $d^{(J)}_{\tilde{m}_J, m_J}(\theta)$ [31], with θ denoting the angle between the microwave electric field and the internuclear axis. The molecular states in the rotated frame take the form:

$$|\tilde{\psi}_{\text{mol}}(R, \theta)\rangle = \frac{1}{\sqrt{2}} \sum_{\tilde{\lambda}_a \tilde{\lambda}_b} C_{\tilde{\lambda}_a, \tilde{\lambda}_b}(R, \theta)$$
$$\times [|\tilde{\lambda}_a \tilde{\lambda}_b\rangle - p(-1)^{\ell_a + \ell_b}|\tilde{\lambda}_b \tilde{\lambda}_a\rangle], \quad (2)$$

with the transformed coefficients:

$$C_{\tilde{\lambda}_a, \tilde{\lambda}_b}(R, \theta) = \sum_{m_{J_a}, m_{J_b}} c_{\lambda_a, \lambda_b}(R) d^{(J_a)}_{\tilde{m}_{J_a}, m_{J_a}}(\theta) d^{(J_b)}_{\tilde{m}_{J_b}, m_{J_b}}(\theta). \quad (3)$$

There, single-atom base kets in the molecular frame:

$$\lambda_{a(b)} = |n_{a(b)}, \ell_{a(b)}, J_{a(b)}, m_{J_{a(b)}}\rangle,$$

and the frame of the microwave field:

$$\tilde{\lambda}_{a(b)} = |n_{a(b)}, \ell_{a(b)}, J_{a(b)}, \tilde{m}_{J_{a(b)}}\rangle,$$

only differ in magnetic quantum numbers. The sum in Eq. (3) is restricted by $|m_{J_{a(b)}}| \leqslant J_{a(b)}$ and $m_{J_a} + m_{J_b} = M$, while the ranges in $\tilde{m}_{J_{a(b)}}$ are only limited by $|\tilde{m}_{J_{a(b)}}| \leqslant J_{a(b)}$. We next compute R- and θ-dependent microwave excitation rates on the adiabatic molecular potentials by taking the squares of electric-dipole microwave-excitation matrix elements between precursor pair states $[(n + 2)D_{5/2}]_2$ and rotated target pair states $(n + 2)D_{5/2}nF_J$.

The $(n + 2)D_{5/2}nF_J$ target pair states are generally configuration and FS mixed. In contrast, at the R values of interest,

the $[(n + 2)D_{5/2}]_2$ precursor pair states exhibit no significant configuration mixing and only show small, positive van der Waals level shifts of $\lesssim 2$ MHz. Therefore, we simplify the computation of the R- and θ-dependent microwave excitation rates by using optically excited, noninteracting $[(n + 2)D_{5/2}]_2$ pair states as an approximation for the precursor pair states.

The R- and θ-dependent microwave excitation rates are then averaged over θ using the isotropic weighting function $\sin(\theta)/2$ for the molecular alignment, with θ ranging from 0 to π. This yields R-dependent isotropic microwave transition rates on the adiabatic potentials. These are used for the symbol areas in Fig. 2(a).

Finally, the R-dependent isotropic microwave transition rates on the adiabatic potentials are sampled along the R axis in Fig. 2(a) and summed over the adiabatic potentials for all M and p to produce spectra that depend on microwave frequency. These spectra model experimental data such as in Fig. 2(b). In the spirit of a two-body approximation, in the radial sampling, we ignore contributions involving interactions between more than two atoms. We therefore use a radial weighting function given by the nearest-neighbor distribution in an ideal gas $(3/r)(R/r)^2 \exp[-(R/r)^3]$, where r denotes the Wigner-Seitz radius.

Typical θ-averaged and R-integrated microwave spectra are shown in Fig. 2(c) for two indicated values of the Wigner-Seitz radius. The model spectra reproduce the essential features measured in Fig. 2(b), except that the measured features attributed to the $(n + 2)D_{5/2}nF_J$ molecules appear to be downshifted by 1–2 MHz relative to the computed ones. We believe that this shift is caused by the positive $\lesssim 2$ MHz van der Waals shifts of the precursor pair state, which result in negative shifts of the measured molecular peaks by an equal amount. Thus, the measured spectrum in Fig. 1(b) exhibits energy shifts that are caused by the energy distribution of the Rydberg-pair sample on the unbound, repulsive precursor potential $[(n + 2)D_{5/2}]_2$. Under this assumption, Franck-Condon overlaps between the free and bound vibrational states would play a role in microwave photo-association spectroscopy of Rydberg macro-dimers.

V. FRANCK-CONDON EFFECTS

Our findings in the previous section suggest that the energy of the $[(n + 2)D_{5/2}]_2$ precursor pair state on its repulsive interaction potential may be tuned to maximize the Franck-Condon overlap for the microwave transitions. To study this possibility, we have varied the detuning of the 509 nm laser to the blue side of atomic $nD_{5/2}$ resonances during the precursor-state preparation. For $n = 48$, we have observed a net improvement of the molecular signal at ~200 kHz blue detuning. This suggests that, by energy tuning of the turning point of the precursor state relative to the peak(s) of the macro-dimer wave function, one can maximize the macro-dimer production rates, as indicated by the wave function sketches in Fig. 1(c).

Presently, the efficacy of this type of Franck-Condon tuning is hampered by the width of the initial kinetic energy distribution of the atoms, which translates into a frequency uncertainty on the order of 1 MHz on the incident $[(n + 2)D_{5/2}]_2$ potential. Also, the optical blue detuning on the repulsive $[(n + 2)D_{5/2}]_2$ potential leads to both a general
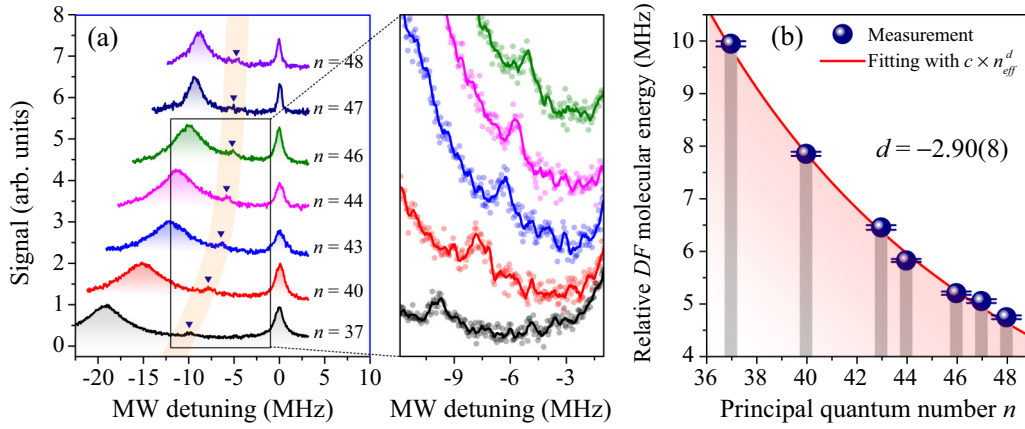
FIG. 4. (a) Microwave spectra, showing interaction-broadened atomic nF_J lines (tall peaks on the left and right) and $(n + 2)D_{5/2} nF_J$ macro-dimer signals (highlighted peaks between the atomic lines) for $37 \leqslant n \leqslant 48$. In the inset, we display enlarged plots of the macro-dimer signals for $n = 37-46$. (b) Measurements (symbols) of the energies of the macro-dimer peaks relative to the $nF_{5/2}$ atomic lines as a function of n. The solid red line shows an allometric fit with fit parameters as indicated.

decrease of the launch-state Rydberg-atom density as well as an enhanced Rydberg-atom repulsion. Both effects are detrimental to the net macro-dimer excitation probability by the subsequent microwave pulse. Hence, our observation of a moderate molecular-signal enhancement when blue detuning the Rydberg excitation laser already is highly encouraging.

VI. MACRO-DIMER ENERGIES VS n

From microwave spectra analogous to Fig. 2(b), we have extracted the energy of the most prominent molecular $(n + 2)D_{5/2} nF_J$ peaks relative to the $nF_{5/2}$ atomic lines for $37 \leqslant n \leqslant 48$. The magnitudes of the relative line positions, extracted from the spectra displayed in Fig. 4(a) and plotted against n in Fig. 4(b), closely follow an allometric fit of the form $y = c\, n_{\mathrm{eff}}^d$. Our fit result $d = -2.90(8)$ means that the line positions track closely in proportion with the FS splitting. Macro-dimer energy scalings near n^{-3} have been observed elsewhere [19,32,33]. The data and scalings observed in Fig. 4 show that the FS-mixed $(n + 2)D_{5/2} nF_J$ macro-dimers are generic and exist over a substantial range of n. The molecular potentials and the widths of the macro-dimer peaks in Figs. 2 and 4 further show that the depths of the molecular-potential wells (i.e., the molecular binding energies) are ∼25% of the relative line positions shown in Fig. 4(b).

VII. STARK EFFECT OF MACRO-DIMERS

Next, we have measured the Stark effect of $39D_{5/2} 37F_J$ Rydberg macro-dimers in a weak applied static electric field E_{DC}. In Fig. 5(a), we show a contour plot of spectra vs E_{DC} and microwave detuning. In Figs. 5(b)–5(d), we present Stark shifts of the atomic and molecular peaks, obtained from Lorentzian fits to the respective peaks in Fig. 5(a). Both atomic and molecular lines are redshifted due to the quadratic Stark effect. The fitted polarizabilities of the transition frequencies, defined as the differences between the level polarizabilities of the upper and lower states of the microwave transitions, are given in Table I.

For the atomic lines in Fig. 5, our calculations (see Appendix A) yield an isotropic average of the transition polarizabilities of ≈85 kHz/(V/m)², which agrees with the measurements in Table I within uncertainties.

Unexpectedly, the measured transition polarizability of the molecular line α_M is ∼2.5 times larger than the transition polarizabilities of the atomic lines (see Table I). In the following, we compare the measured molecular transition polarizability α_M with the results of a corresponding calculation, denoted $\alpha_{M,T}$. In a perturbative picture, which should apply if the molecular Stark shift is much less than the binding energy (a few megahertz in our case), the leading contribution to the molecular polarizability is the sum of the polarizabilities of the atomic constituents. This yields (absolute) theoretical molecular polarizabilities on the adiabatic molecular potentials of

$$\tilde{\alpha}_{0,M,T}(R, \theta) = \sum_{\tilde{\lambda}_a \tilde{\lambda}_b} |C_{\tilde{\lambda}_a, \tilde{\lambda}_b}(R, \theta)|^2 [\alpha(\tilde{\lambda}_a) + \alpha(\tilde{\lambda}_b)]. \quad (4)$$

There, $\alpha(\tilde{\lambda})$ are the absolute polarizabilities of the atomic-constituent states $|\tilde{\lambda}\rangle$. The atomic polarizabilities are obtained as described in Appendix A. The coefficients $C_{\tilde{\lambda}_a, \tilde{\lambda}_b}$ are taken from Eq. (3). The results $\tilde{\alpha}_{0,M,T}(R, \theta)$ are averaged over θ with the normalized weighting function $\sin(\theta)/2$, yielding an isotropic average $\alpha_{0,M,T}(R)$.

In the computations for Fig. 2(a), we have found that, within the macro-dimer potential wells, the wave functions from Eq. (1) exhibit no significant ℓ mixing with $\ell \geqslant 4$ states. Under the absence of ℓ mixing, it is $\alpha_{0,M,T}(R) = \alpha_s(37F_J) + \alpha_s(39D_{5/2})$ with the scalar polarizabilities α_s from Table II,

TABLE I. Transition polarizabilities in kHz/(V/m)² for the spectral lines listed in the first column.

Line	α
$37F_{5/2}$	88(06)
$37F_{7/2}$	75(12)
$[39D_{5/2}\, 37F_J]$	210(18)
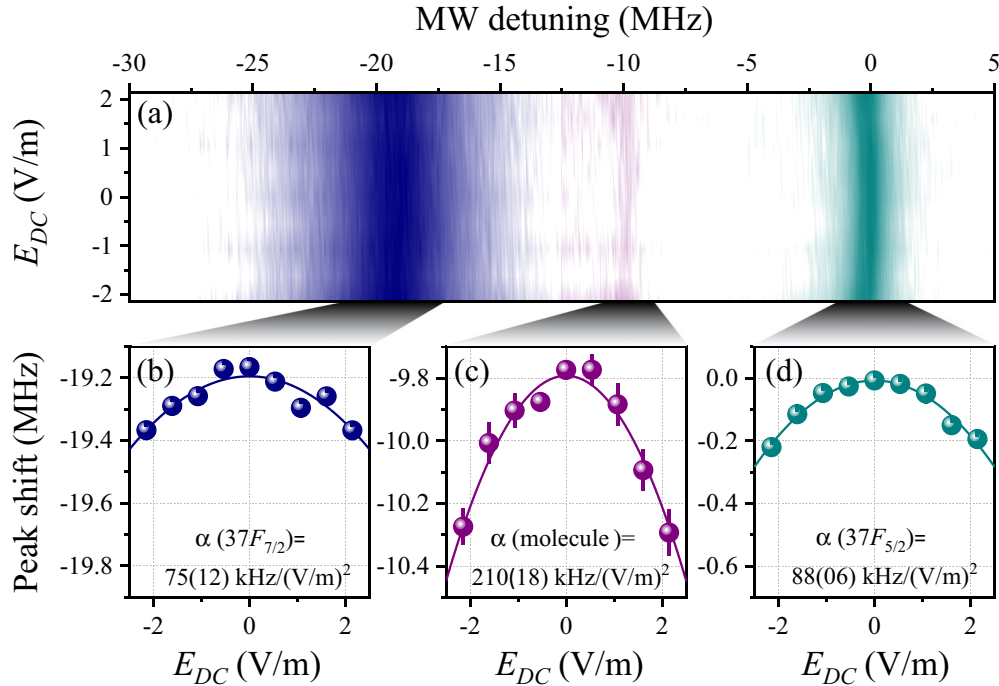
FIG. 5. (a) Color-scale plot of microwave spectra near $37F_J$ vs DC electric field E_{DC} and microwave detuning from the atomic $39D_{5/2} \rightarrow 37F_{5/2}$ transition. Symbols in the bottom panels show (b) Stark shifts of the atomic line $37F_{7/2}$, (c) the $39D_{5/2}$ $37F_J$ Rydberg macro-dimer, and (d) the atomic line $37F_{5/2}$. The solid lines show best-fit functions of the type $W = -(\frac{1}{2})\alpha E_{DC}^2 + \beta$, with fitted transition polarizabilities α shown in the panels.

reflecting the fact that the molecule contains one $39D_{5/2}$ atom and one $37F_J$ atom. Since the J dependence of $\alpha_s(37F_J)$ is minimal, the R dependence of $\alpha_{0,M,T}(R)$ due to R-dependent FS mixing (see Fig. 3) is minimal, and the transition polarizability is $\alpha_{M,T} \approx \alpha_s(37F) + \alpha_s(39D_{5/2}) - 2 \times \alpha_s(39D_{5/2})$. There, the subtracted term accounts for the polarizability of the configuration-mixing-free precursor state $[39D_{5/2}]_2$ of the microwave transition. Hence, without substantial ℓ mixing and in the assumed perturbative picture, the theoretical transition polarizability of the macro-dimer is $\alpha_{M,T} \approx \alpha_s(37F) - \alpha_s(39D_{5/2}) \approx 85$ kHz/(V/m)^2, the same as for the atomic lines. This value of $\alpha_{M,T}$ is about a factor of 2.5 smaller than the measured $\alpha_M = 210(18)$ kHz/(V/m)^2.

The discrepancy could be due to configuration admixtures from highly polarizable $\ell \geqslant 4$ states, which may only appear in calculations when using larger basis sets. Increasing our basis sets to include atomic states with $\ell \leqslant 15$ and pair states with energy defects $|\Delta_2| \leqslant h \times 50$ GHz, there is evidence that the macro-dimer states pick up an increasing (but still too small) high-ℓ character (see Appendix B). It remains to be seen in future work, which is beyond the scope of this paper, whether calculations with even larger basis sets will yield molecular polarizabilities in agreement with the measured α_M. Also, the validity of the utilized perturbative weak-field model for the molecular polarization could be tested.

VIII. STARK BROADENING OF MACRO-DIMER SIGNALS

From Fig. 5, we also obtain the linewidths of the atomic and molecular lines. In Fig. 6(a), we show the linewidths measured for a selection of atomic and molecular peaks as

a function of the applied electric field E_{DC}. The atomic lines are fairly broad throughout, in agreement with Fig. 2. As a
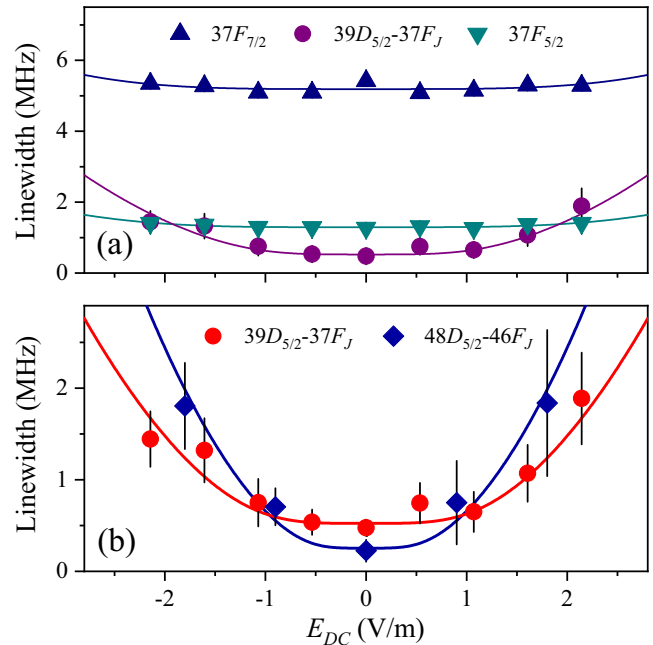
FIG. 6. (a) Linewidths of the atomic $37F_{7/2}$ (navy) and $37F_{5/2}$ (dark cyan) peaks, and of the molecular $39D_{5/2}$ $37F_J$ (purple) peak from Fig. 5 vs E_{DC}. (b) Line broadening of the molecular $39D_{5/2}$ $37F_J$ (red) and $48D_{5/2}$ $46F_J$ (royal) molecular peaks vs E_{DC}. In both (a) and (b), solid curves are best fits of the form $a\sqrt{1 + b E_{DC}^4}$.

result, any extra broadening that occurs with increasing $|E_{DC}|$ is insignificant. In contrast, the molecular feature is narrow at $E_{DC} \sim 0$, in agreement with Fig. 2, and there is considerable extra broadening with increasing $|E_{DC}|$. In the following, we investigate the Stark broadening of the molecular signals.

The variation of the molecular Stark shift is $\delta W_S = -\alpha_M E_{DC}\delta E_{DC} - E_{DC}^2 \delta \alpha_M / 2$. Here, the field variation δE_{DC}, caused by electric field inhomogeneity, is proportional to E_{DC} and is very small. The variation of the molecular polarizability $\delta \alpha_M$ is caused by the isotropic distribution of the molecular-alignment angle θ, which broadens the distribution in $\tilde{m}_J$. This leads to a variation $\delta \alpha_M$ through to the tensor polarizabilities of the contributing atomic states (see Appendix A). We estimate the resultant $\delta \alpha_M \sim \pm 0.25 \alpha_M$, equivalent to an estimated $\delta W_S / W_S \sim \pm 0.25$. As seen in Fig. 6(b), at the largest probed $|E_{DC}|$, the net molecular linewidth δW is much larger than the background linewidth δW_0 observed at $E_{DC} = 0$. Hence, for an observed net linewidth $\delta W = \sqrt{\delta W_0^2 + \delta W_{S,A}^2}$, at the largest probed $|E_{DC}|$, the observed Stark broadening $\delta W_{S,A} \approx \delta W$. Taking half the maximum width seen in Fig. 6(b), the observed Stark broadening amounts to $\delta W_{S,A} \approx \pm 0.75$ MHz. The maximum shift itself is $W_{S,A} \approx 0.5$ MHz, as seen in Fig. 5(c). The experimental observation therefore is $\delta W_{S,A} / W_{S,A} \sim \pm 1.5$, which greatly exceeds the above estimate $\delta W_S / W_S \sim \pm 0.25$. Hence, there must be unaccounted-for Stark broadening effects that add to the Stark-shift variations caused by atomic tensor polarizability and random molecular alignment.

A permanent molecular dipole moment at zero electric field p_M could, in principle, explain the large observed $\delta W_{S,A}$. However, the $\gtrsim h \times 10$ MHz strength of Rydberg-pair interactions enforces symmetrized pair states at $E_{DC} = 0$, which have well-defined parity [see Eqs. (1) and (2)] and therefore must have $p_M = 0$. As such, the situation differs from Rydberg-ground molecules, which have extremely weak flip interactions and do allow nonsymmetrized pair states with $p_M \neq 0$ [1,7,10].

As another explanation for excess Stark broadening, we consider intramolecular dipole-dipole interactions, which could be a possible source for the observed large values of $\delta W_{S,A}$. The induced intramolecular dipoles are parallel to E_{DC} and form an angle θ relative to the internuclear axis. For constituent polarizabilities estimated at $\alpha_M / 2$ (i.e., half the total molecular polarizability of the symmetrized state), the induced dipole-dipole interaction is $W_I = E_{DC}^2 (\alpha_M^2/4)(1 - 3\cos^2\theta)/(4\pi\epsilon_0 R^3)$. Using the normalized isotropic probability distribution for θ, $P(\theta) = \sin(\theta)/2$, one can verify that the isotropic average of W_I is zero. However, the variation range of $W_I(R, \theta)$ over the full range of θ is large and amounts to $\delta W_I(R) = 3E_{DC}^2 \alpha_M^2/(16\pi\epsilon_0 R^3)$. For $39D_{5/2} 37F_J$ at $R = 2$ μm, it is $\delta W_I \gtrsim h \times 100$ kHz. For a given vibrational state with vibrational wave function $\phi_v(R)$, the value of δW_I would be higher because, in the vibrational average:

$$\langle \delta W_I \rangle = \frac{3E_{DC}^2 \alpha_M^2}{16\pi\epsilon_0} \int \frac{|\phi_v(R)|^2}{R^3} dR, \qquad (5)$$

the short-distance contributions would dominate and drive the average up. Hence, induced dipole-dipole interactions may

add to the Stark linewidths and help explain the results in Figs. 5 and 6.

Since both the discussed $\delta W_{S,A}$ and δW_I scale as E_{DC}^2, the net linewidths in Fig. 6 should follow a function $\delta W = a\sqrt{1 + bE_{DC}^4}$. This function, applied in Fig. 6, fits the data indeed quite well, lending some credibility to the described model.

IX. CONCLUSIONS

In summary, we have observed FS-induced $(n + 2)D_{5/2} nF_J$ Cs Rydberg macro-dimers, modeled the data, and explained the formation mechanisms of these molecules. Different from the commonly used method of laser photo-association, we have employed microwave photo-association, which is narrow band and sensitive to van der Waals interactions of the precursor Rydberg-pair states. Future research will be required to explain the factor of 2.5 discrepancy between measured and calculated macro-dimer polarizabilities, which we have observed in this paper. Important effects may include high-ℓ mixing and higher-order perturbations. Intramolecular induced-dipole-dipole interactions in Rydberg macro-dimers, for which we have found indications, may also deserve additional work. Improvements of the Franck-Condon tuning discussed in Sec. V may be achieved by reducing the atom temperature and by preparing the precursor-state $[nD_{5/2}]_2$ atom pairs on a potential that is structured via a Rydberg-atom optical lattice [34–36].

Improved atom cooling, trapping, and sample preparation methods may be combined with Franck-Condon-tuned microwave photo-association spectroscopy to match the present vibrational resolution of laser photo-association [20–22], to address the adverse effects of atom repulsion on the precursor potentials, and to perform Franck-Condon-sensitive Rydberg macro-dimer spectroscopy. The research may reveal detailed vibrational structures suitable to test and improve models for Born-Oppenheimer potentials, including the effect of nonadiabatic couplings on vibrational-level energies and lifetimes.

APPENDIX A: ATOMIC ELECTRIC POLARIZABILITIES

We compute the DC electric polarizabilities of Rydberg states using private Fortran codes. For the main atomic constituents of the $39D_{5/2} 37F_J$ macro-dimers in Figs. 1 and 5, the polarizabilities are listed in Table II.

TABLE II. Scalar (middle column) and tensor (right column) DC polarizabilities in kHz/(V/m)^2 for the atomic states listed in the first column.

State	a_s	a_t
$39D_{5/2}$	−11.7	13.0
$37F_{5/2}$	75.3	−26.4
$37F_{7/2}$	74.7	−30.5

We recite that, for a given m_J, with the direction of E_{DC} taken as the quantization axis, the polarizability is

$$\alpha(\lambda) = a_{s,\lambda} + a_{t,\lambda}\left[3m_J^2 - J(J+1)\right]/J/(2J-1). \quad (A1)$$

The absolute level shifts are $W(\lambda) = -(\frac{1}{2})\alpha(\lambda)E_{DC}^2$, where $|\lambda\rangle$ is shorthand for the quantum states $|n, \ell, J, m_J\rangle$ in the E_{DC} frame (left column in Table I). The atomic $37F_J$ lines in Fig. 5 are expected to shift according to the transition polarizability for the transition from the lower $39D_{5/2}$ to the upper $37F_J$ states, averaged over m_J. Recalling that the isotropic averages of the tensor polarizabilities are zero, the average transition polarizabilities are ≈85 kHz/(V/m)^2 for both $37F_{5/2}$ and $37F_{7/2}$. This agrees within uncertainties with the values derived from the fits to the Stark shifts of the atomic lines in Fig. 5.

APPENDIX B: MOLECULAR ELECTRIC POLARIZABILITIES

In Fig. 7, we show the isotropic molecular polarizability $\alpha_{0,M,T}(R)$ on the $M = 3$, $p = -1$ potential for the $39D_{5/2}37F_J$ macro-dimer. In the computation, we obtain the isotropic average of Eq. (4), including atomic states with ℓ up to 15.

The FS mixing at $R \sim 2\,\mu m$ causes an ≈1% increase in $\alpha_{0,M,T}(R)$. Near the inner turning point of the potential well R_{min}, the polarizability begins to rise further due to configu-
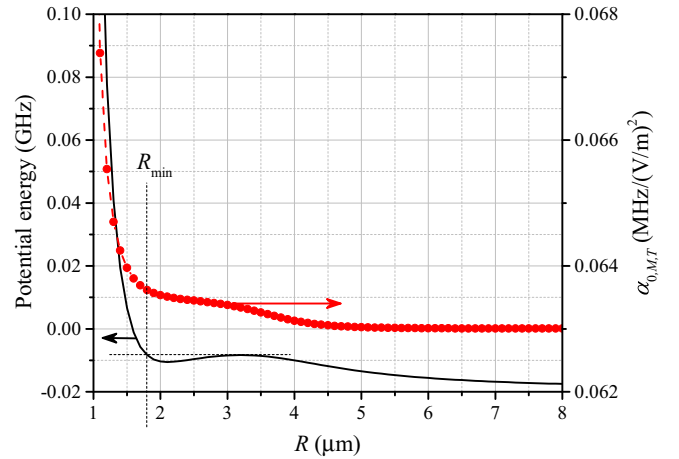
FIG. 7. Isotropic molecular polarizability on the adiabatic potential for $39D_{5/2}37F_J$ with $M = 3$, $p = -1$. Solid black curve: Adiabatic potential vs R. The inner turning point R_{min} of the well that supports macro-dimers is indicated. Red symbols: Isotropic molecular polarizability $\alpha_{0,M,T}(R)$.

ration mixing with $\ell \geqslant 4$ states. For a given vibrational state with vibrational wave function $\phi_\nu(R)$, the isotropic molecular polarizability would be

$$\alpha_\nu = \int_0^\infty |\phi_\nu(R)|^2 \alpha_{0,M,T}(R)dR. \quad (B1)$$

For an explanation of the large measured value of α_M, it would be sufficient for $\alpha_{0,M,T}(R)$ to become (very) large near the inner turning point of $\phi_\nu(R)$, where the ℓ mixing is largest. In view of Fig. 7, it is very clear, however, that any average over vibrational states according to Eq. (B1) will not explain the experimentally observed large values of α_M. It is beyond the scope of this paper to explore the behavior with even larger basis sets.

[1] C. H. Greene, A. S. Dickinson, and H. R. Sadeghpour, Creation of polar and nonpolar ultra-long-range Rydberg molecules, Phys. Rev. Lett. **85**, 2458 (2000).

[2] E. L. Hamilton, C. H. Greene, and H. R. Sadeghpour, Shape-resonance-induced long-range molecular Rydberg states, J. Phys. B: At., Mol. Opt. Phys. **35**, L199 (2002).

[3] A. A. Khuskivadze, M. I. Chibisov, and I. I. Fabrikant, Adiabatic energy levels and electric dipole moments of Rydberg states of Rb$_2$ and Cs$_2$ dimers, Phys. Rev. A **66**, 042709 (2002).

[4] V. Bendkowsky, B. Butscher, J. Nipper, J. Shaffer, R. Löw, and T. Pfau, Observation of ultralong-range Rydberg molecules, Nature (London) **458**, 1005 (2009).

[5] D. A. Anderson, S. A. Miller, and G. Raithel, Photoassociation of long-range nD Rydberg molecules, Phys. Rev. Lett. **112**, 163201 (2014).

[6] A. T. Krupp, A. Gaj, J. B. Balewski, P. Ilzhöfer, S. Hofferberth, R. Löw, T. Pfau, M. Kurz, and P. Schmelcher, Alignment of D-state Rydberg molecules, Phys. Rev. Lett. **112**, 143008 (2014).

[7] D. Booth, S. T. Rittenhouse, J. Yang, H. R. Sadeghpour, and J. P. Shaffer, Production of trilobite Rydberg molecule dimers

with kilo-Debye permanent electric dipole moments, Science **348**, 99 (2015).

[8] T. Niederprüm, O. Thomas, T. Eichert, C. Lippe, J. Pérez-Ríos, C. H. Greene, and H. Ott, Observation of pendular butterfly Rydberg molecules, Nat. Commun. **7**, 12820 (2016).

[9] H. Saßmannshausen, F. Merkt, and J. Deiglmayr, Experimental characterization of singlet scattering channels in long-range Rydberg molecules, Phys. Rev. Lett. **114**, 133201 (2015).

[10] S. Bai, X. Han, J. Bai, Y. Jiao, J. Zhao, S. Jia, and G. Raithel, Cesium $nD_J + 6S_{1/2}$ Rydberg molecules and their permanent electric dipole moments, Phys. Rev. Res. **2**, 033525 (2020).

[11] A. Duspayev, X. Han, M. A. Viray, L. Ma, J. Zhao, and G. Raithel, Long-range Rydberg-atom–ion molecules of Rb and Cs, Phys. Rev. Res. **3**, 023114 (2021).

[12] M. Deiß, S. Haze, and J. Hecker Denschlag, Long-range atom-ion Rydberg molecule: A novel molecular binding mechanism, Atoms **9**, 34 (2021).

[13] N. Zuber, V. Anasuri, M. Berngruber, Y.-Q. Zou, F. Meinert, R. Löw, and T. Pfau, Observation of a molecular bond between ions and Rydberg atoms, Nature (London) **605**, 453 (2022).

[14] Y.-Q. Zou, M. Berngruber, V. S. V. Anasuri, N. Zuber, F. Meinert, R. Löw, and T. Pfau, Observation of vibrational dynamics of oriented Rydberg-atom-ion molecules, Phys. Rev. Lett. **130**, 023002 (2023).

[15] C. Boisseau, I. Simbotin, and R. Côté, Macrodimers: Ultralong range Rydberg molecules, Phys. Rev. Lett. **88**, 133004 (2002).

[16] K. R. Overstreet, A. Schwettmann, J. Tallant, D. Booth, and J. P. Shaffer, Observation of electric-field-induced Cs Rydberg atom macrodimers, Nat. Phys. **5**, 581 (2009).

[17] J. Deiglmayr, H. Saßmannshausen, P. Pillet, and F. Merkt, Observation of dipole-quadrupole interaction in an ultracold gas of Rydberg atoms, Phys. Rev. Lett. **113**, 193001 (2014).

[18] H. Saßmannshausen and J. Deiglmayr, Observation of Rydberg-atom macrodimers: Micrometer-sized diatomic molecules, Phys. Rev. Lett. **117**, 083401 (2016).

[19] X. Han, S. Bai, Y. Jiao, L. Hao, Y. Xue, J. Zhao, S. Jia, and G. Raithel, Cs $62D_J$ Rydberg-atom macrodimers formed by long-range multipole interaction, Phys. Rev. A **97**, 031403(R) (2018).

[20] S. Hollerith, J. Zeiher, J. Rui, A. Rubio-Abadal, V. Walther, T. Pohl, D. M. Stamper-Kurn, I. Bloch, and C. Gross, Quantum gas microscopy of Rydberg macrodimers, Science **364**, 664 (2019).

[21] S. Hollerith, K. Srakaew, D. Wei, A. Rubio-Abadal, D. Adler, P. Weckesser, A. Kruckenhauser, V. Walther, R. van Bijnen, J. Rui *et al.*, Realizing distance-selective interactions in a Rydberg-dressed atom array, Phys. Rev. Lett. **128**, 113602 (2022).

[22] S. Hollerith and J. Zeiher, Rydberg macrodimers: Diatomic molecules on the micrometer scale, J. Phys. Chem. A **127**, 3925 (2023).

[23] M. Kiffner, H. Park, W. Li, and T. F. Gallagher, Dipole-dipole-coupled double-Rydberg molecules, Phys. Rev. A **86**, 031401(R) (2012).

[24] X. Han, S. Bai, Y. Jiao, G. Raithel, J. Zhao, and S. Jia, Adiabatic potentials of cesium $(nD_J)_2$ Rydberg-Rydberg macrodimers, J. Phys. B: At., Mol. Opt. Phys. **52**, 135102 (2019).

[25] T. F. Gallagher, *Rydberg Atoms*, Cambridge Monographs on Atomic, Molecular and Chemical Physics (Cambridge University Press, Cambridge, 1994).

[26] K. Singer, M. Reetz-Lamour, T. Amthor, L. G. Marcassa, and M. Weidemüller, Suppression of excitation and spectral broadening induced by interactions in a cold gas of Rydberg atoms, Phys. Rev. Lett. **93**, 163001 (2004).

[27] A. Jahangiri, J. P. Shaffer, L. F. Gonalves, and L. G. Marcassa, Anisotropic interactions in electric field polarized ultracold Rydberg gases, J. Phys. B: At., Mol. Opt. Phys. **53**, 014001 (2019).

[28] S. Hollerith, V. Walther, K. Srakaew, D. Wei, D. Adler, S. Agrawal, P. Weckesser, I. Bloch, and J. Zeiher, Rydberg molecules bound by strong light fields, arXiv:2401.05129.

[29] J. Bai, R. Song, J. Fan, Y. Jiao, J. Zhao, S. Jia, and G. Raithel, Quantum defects of nF_J levels of Cs Rydberg atoms, Phys. Rev. A **108**, 022804 (2023).

[30] S. Weber, C. Tresp, H. Menke, A. Urvoy, O. Firstenberg, H. P. Büchler, and S. Hofferberth, Calculation of Rydberg interaction potentials, J. Phys. B: At., Mol. Opt. Phys. **50**, 133001 (2017).

[31] J. J. Sakurai and J. Napolitano, *Modern Quantum Mechanics*, 3rd ed. (Cambridge University Press, Cambridge, 2020).

[32] N. Samboy, J. Stanojevic, and R. Côté, Formation and properties of Rydberg macrodimers, Phys. Rev. A **83**, 050501(R) (2011).

[33] N. Samboy and R. Côté, Rubidium Rydberg macrodimers, J. Phys. B: At., Mol. Opt. Phys. **44**, 184006 (2011).

[34] V. S. Malinovsky, K. R. Moore, and G. Raithel, Modulation spectroscopy of Rydberg atoms in an optical lattice, Phys. Rev. A **101**, 033414 (2020).

[35] R. Cardman and G. Raithel, Driving alkali Rydberg transitions with a phase-modulated optical lattice, Phys. Rev. Lett. **131**, 023201 (2023).

[36] B. Ravon, P. Méhaignerie, Y. Machu, A. D. Hernández, M. Favier, J. M. Raimond, M. Brune, and C. Sayrin, Array of individual circular Rydberg atoms trapped in optical tweezers, Phys. Rev. Lett. **131**, 093401 (2023).